Imaging the Photoionization of Individual CdSe/CdS Core−Shell Nanocrystals on n- and p-Type Silicon Substrates with Thin Oxides

Oksana Cherniavskaya, Liwei Chen, and Louis Brus*

Columbia University, Department of Chemistry, 3000 Broadway, New York, New York 10027

Received: September 29, 2003; In Final Form: December 16, 2003

The low-intensity photoionization of individual semiconductor nanocrystals, at 23 °C in dry nitrogen, is time-resolved over many hours for both S (532-nm excitation) and P (395-nm excitation) nanocrystal excited states using electrostatic force microscopy. Over 7000 calibrated charge measurements have been made on 14- and 21-Å-thick oxide layers. Photoexcited electrons tunnel across the oxide into the silicon, and multiple charges can build up on individual nanocrystals at intensities of only $0.1-0.01$ W/cm^2. The silicon dopant type influences the net nanocrystal charging via the interfacial band bending; P-type subtrates show a faster nanocrystal reneutralization rate due to their higher interfacial electron concentration. There is a huge range of photoionzation behavior for individual nanocrystals. This behavior is different for 395- and 532-nm excitation in the same nanocrystal. This individuality seems in part to reflect tunneling through spatially localized defect states in the oxide. The line widths of spatial charge images of individual nanocrystals and the semicontinuous rate of charge re-neutralization after excitation suggest that we observe trapped electron motion in the adjacent oxide and/or on the nanocrystal surface, in addition to the ionized nanocrystal. On average, tunneling of the excited P electron is faster by $1-2$ orders of magnitude than that of the S electron; the data show direct photoionization from the excited P state. A kinetic model is developed, including the effect of charging energy on tunneling rate, and applied to ensemble average behavior. There is no quantitative agreement of the tunneling-rate dependence on oxide thickness and excitation energy with the simple 1D effective mass tunneling model. However, overall observed trends are rationalized in light of current thin-oxide tunneling literature.

1. Introduction

The fluorescence intermittency of semiconductor nanocrystals remains imperfectly understood despite a systematic research effort since the first observation in 1996.[1] Luminescence blinking and spectral diffusion in some way reflect charge redistribution and/or photoionization.[2−7] The weak temperature dependence suggests direct tunneling to trap states. Even in the best core/shell nanocrystals currently synthesized, the observation of inverse power law kinetics over many decades implies that a wide range of trap states are weakly coupled, with fluctuating matrix elements, to the optically excited internal state. A consideration of tunneling rates implies that the states responsible for the longer on and off times are not in the nanocrystal but $1-2$ nm away in the neighborhood, perhaps in the amorphous silica coverslip substrate.[8−10] Thus, rare "blinking" events on the second to hour time scale are a long-distance probe of the nanocrystal's electrical environment. It is important to understand this effect because the nanocrystal charge state strongly infuences electrical transport properties in photovoltaic and electroluminescent devices, optical gain in nanocrystal lasers, and photostability in biological imaging.[11−13]

In this paper, we directly characterize nanocrystal photoionization and neutralization on silica surfaces using electrostatic force microscopy (EFM). Our approach is complimentary to the luminescence experiments; taken together the two experiments yield a more complete understanding of nanocrystal photophysics and charge equilibrium on surfaces. EFM involves capacitive coupling between a metalized local probe tip and a conducting ground plane. We use a doped crystalline Si wafer as the ground plane and place the nanocrystals on $1-2$-nm-thick surface oxide layers. In this context, the Si itself is a special type of "trap state" whose Fermi energy can be varied by doping. In fact, in a preliminary letter we observed a strong dependence of photoionization on Si doping, indicating that electrons photoionize and tunnel across the oxide.[14] EFM allows the simultaneous mapping of topography and electrostatic field gradients above the surface. With modeling and calibration,[15] EFM provides a direct measurement of sample charge and polarizability. We quantitatively study nanocrystal photoionization as a function of irradiation wavelength, oxide thickness, and doping. Because we observe a wide distribution of behavior for individual nanocrystals, we describe the data in some detail.

2. EFM Theory

A conductive AFM probe in Figure 1 is electrically connected to a conductive substrate, forming a capacitor. The topography of the sample is recorded on the first pass of a given line (in tapping mode), with no bias applied between the surface and the probe. On the second pass, the probe is lifted a set amount, z_{lift} (Figure 1), above the surface and scanned at a constant height while still being dithered mechanically at its natural frequency; also, a voltage is applied between the tip and the substrate. Electric field gradients due to surface charge and dielectric properties are directly recorded by the probe. Using lock-in detection, the apparatus records the shifts in the resonance frequency, ν, of the probe due to these force gradients.[16] When the force gradients are small (in this case on the order of 10^{-3}

Photoionization of CdSe/CdS Nanocrystals

*J. Phys. Chem. B, Vol. 108, No. 16, 2004* **4947**
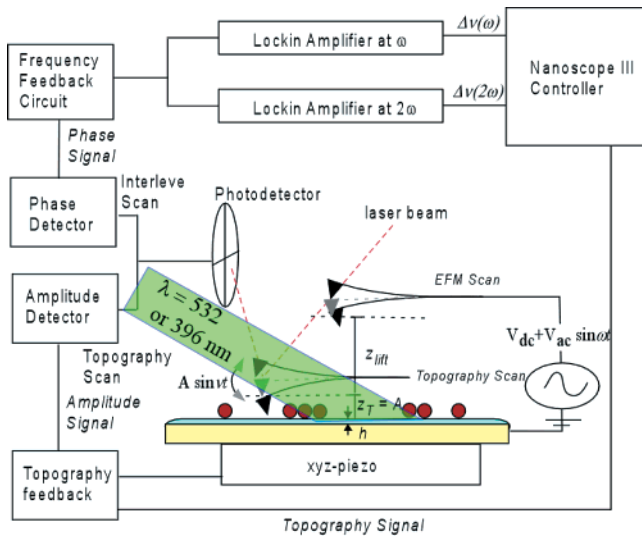
Figure 1. EFM experimental setup. The bottom portion of the flowchart shows that the tapping-mode topographic data is acquired on the first pass of a given line (main scan). The top of the chart represents the second scan of a given line (interleave scan), where the cantilever is lifted a set distance above the surface and scanned at constant height from the substrate while being dithered both mechanically and electrically. The frequency shift of the probe is detected by the phase-lock loop and fed into two external lock-in amplifiers, where the signals at frequencies ω and 2ω are isolated and fed back to the Nanoscope IIIa controller, where the image is created.

N/m), the absolute value of the frequency shift can be related to the force gradient by

$$|\Delta \nu| = |\nu - \nu'| \approx \frac{\nu}{2k}\frac{\partial F}{\partial z} \qquad (1)$$

where k is the cantilever force constant and ν is its natural resonance frequency.

The electrostatic forces arise from two types of interactions: Coulombic interactions of the capacitively charged probe with sample charges and multipoles and capacitive coupling to the substrate. The force due to the sample is the product of the total surface normal electric field from the sample, E_z, and the charge on the tip, Q_{tip}:

$$F_{coul} = E_z Q_{tip} \qquad (2)$$

The force between the plates of the empty capacitor is given by

$$F_{cap} = \frac{1}{2}\frac{dC}{dz}V^2 \qquad (3)$$

where V is the voltage applied between the surface and the tip, $C(z)$ is the empty tip−surface capacitance, and z is the separation of the probe apex from the conductive plane of the substrate. If a potential $V = V_{dc} + V_{ac}\sin(\omega t)$ is applied between the tip and the substrate, then the total voltage drop is $V_{tot} = \varphi + V_{dc} + V_{ac}\sin(\omega t)$, where φ is the contact potential difference and

$$F_{EFM} = \frac{1}{2}\frac{dC}{dz}V_{tot}^2 + E_z Q_{tip} \qquad (4)$$

where $Q_{tip} = CV_{tot} + Q_{im}$ and Q_{im} is the set of images induced in the tip by the charges on the surface. E_z has two components: E_z^S due to static charges, multipoles, and their images in the substrate and $|E_z^d|\sin(\omega t)$ due to oscillating polarization induced in the sample by the ac field. Thus, $E_z = E_z^S + |E_z^d|$

$\sin(\omega t)$ and $|E_z^d| = f(\epsilon(x,y), \{g\})V_{ac}$, where f is determined by the local dielectric constant $\epsilon(x, y)$ and the geometric parameters $\{g\}$ of the system.

There are two oscillating components of the electrostatic force experienced by the probe:[15] one at ω and one at 2ω:

$$F(\omega) = \left((V_{dc} + \varphi)\frac{dC}{dz} + [f(\epsilon, \{g\})(Q_{im} + C(V_{dc} + \varphi)) + \right.$$
$$\left. E_z^S f_{im}(\epsilon, \{g\})] + E_z^S C\right)V_{ac} \quad (5)$$

and

$$F(2\omega) = \left(\frac{1}{2}f(\epsilon, \{g\})C + \frac{1}{4}\frac{dC}{dz}\right)V_{ac}^2 \qquad (6)$$

$F(2\omega)$ is a function only of $C(z)$ and sample polarizability, as previously described.[15] $F(\omega)$ is composed of three terms. The first term is due to the contact potential difference between the probe and the substrate, nulled out by setting $V_{dc} = -\varphi$. The second term is due to the interaction of the oscillating dipole in the sample with the static charges in the tip plus the interaction of the static sample field with the image of the oscillating sample dipoles in the tip. At ac voltage amplitudes and tip−surface separations used in this experiment, this interaction is less than 1% of the total force. The third term is dominant and can be described by

$$F(\omega) = E_z^S C V_{ac} \qquad (7)$$

We derive the force on the tip as it interacts with the surface electric field using a geometrical model of the tip and nanocrystal charge distribution.[15] The parameters of the tip−surface and tip−sample interaction models are described in the Appendix.

3. Experimental Procedure

Chemically synthesized CdS-coated CdSe particles[17] with an average diameter of $\sim$5 nm (stored in mother liquor under a nitrogen atmosphere in the dark) were spin-coated onto degenerately doped P-type (B-doped, 0.001−0.004 Ω cm) and N-type (Sb-doped, 0.008−0.03 Ω cm) silicon substrates with 21- and 14-Å thermal oxide layers (IBM advanced silicon technology laboratory). The thinner oxide was grown in 15% NO and has partial Si_3N_4 character. The thickness of the oxide was measured by electrical (21 and 12 Å) and optical (21 and 16 Å) methods at IBM. The value of 14 was used in tunneling calculations for the thinner oxide. The substrates were cleaned with ethanol and hexane prior to particle deposition. During sample preparation, exposure to air was minimized typically to no more than 10 min to prevent photooxidation.[17−20]

EFM images were collected as described in detail elswhere,[15] at room temperature in a dry box (MBraun Unilab, Simatic OP7; $P(O_2) < 2$ ppm, $P(H_2O) < 1$ ppm) using a Digital Instruments (Santa Barbara, CA) Nanoscope IIIa Multimode AFM with an extender module. A single calibrated Pt−Ir-coated EFM tip (Nanosensor EFM-20) from Molecular Imaging (Phoenix, AZ) was used in all experiments discussed here. Its resonance frequency was 55 kHz, and the spring constant was about 1.35 N/m as determined by the method of Sader et al.[21] Each image took $\sim$12 min to acquire. All images were taken at a resolution of 256 × 256 pixels². During imaging, the V_{dc} was set to zero out the average contact potential between the substrate and the probe. The typical topographic feedback set-point was 0.35 V, and the photodiode sensitivity was 13 nm/V.
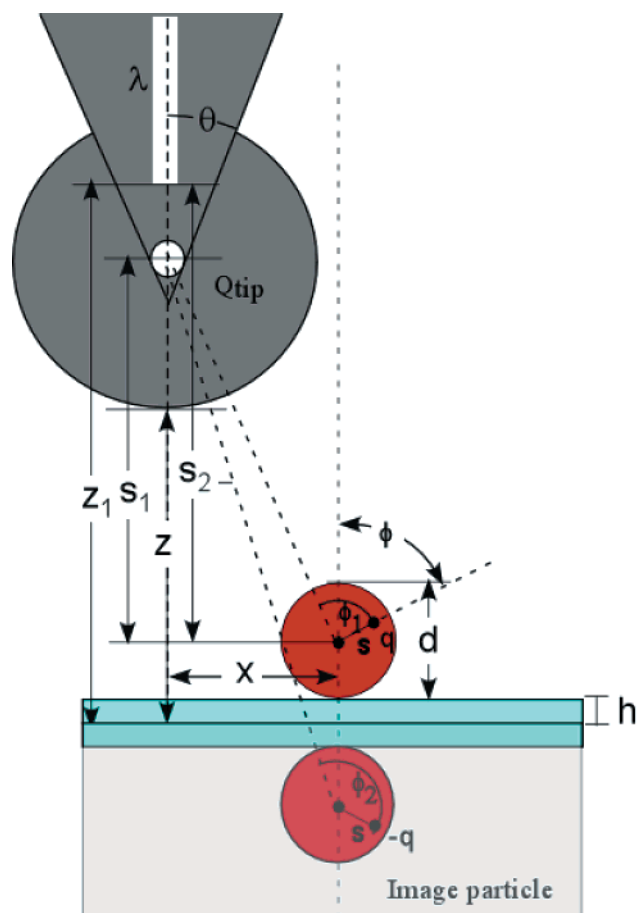
Figure 2. Schematic of the charge distribution in the tip and the sample, indicating the relevant geometric parameters.

Samples were exposed to a grazing angle, 396-nm light from a 4-mW (p-polarized) diode laser (Coherent, RA 0222-583-00) at ~15 mW/cm² or to 532-nm light from a 15-mW (unpolarized) diode laser (Information Unlimited, model LM532P20) at ~60 mW/cm², while being continuously imaged for 4–6 h. No intermediate optics were used between the laser and the sample. After the laser was turned off, the samples were continuously imaged for 15–30 h to observe the time dependence of reneutralization. A total of eight experiments were performed: all ternary combinations of N- and P-type silicon, 14- and 21-Å SiO₂, with 532- and 396-nm excitation. To preserve some consistency in laser alignment between the experiments, they were performed in the following order: first N–Si/21 Å SiO₂ was studied with 532-nm excitation; then the same sample area of P–Si/21-Å SiO₂ was studied with 532-nm followed by 396-nm excitation; then a different area of N–Si/21-Å SiO₂ was studied with 396-nm light. The same order was used for the 14-Å SiO₂ samples. For each image, representing a point in time, the total numbers of charged and uncharged particles were recorded, and approximately 10 particles were chosen whose charge signals were recorded as well. Image data was analyzed using Igor 4.0 (Wavemetrics Inc, Lake Oswego, OR). All mathematical modeling was done using Mathematica 4.0 (Wolfram Research, Champaign, IL).

4. Charge of Individual Nanocrystals

We observed a diversity of behaviors and will describe our observations in some detail. Figures 3 and 4 show one topography image and corresponding charge images for CdSe/CdS nanoparticles at various times on N-type Si/14-Å SiO₂ with 396-nm excitation and on P-type Si /14-Å SiO₂ with 532-nm excitation, respectively. In Figure 3b, we see that before exposure to 396-nm light there is only one nanoparticle showing a charge signal. Once the sample is photoexposed (Figure 3c), many charged particles appear. Equilibrium is reached ~100 minutes into the experiment, as exemplified by an image at $t =$ 180 min (Figure 3d). On P-type Si (Figure 4), more charge is seen prior to photoexposure, equilibrium is reached faster, and charge magnitudes are on average lower than on N-type silicon.

For each analyzed particle, the diameter and the maximum $\Delta \nu(\omega)$ signal above the overall background are measured and used to calculate the charge. The charge magnitude of a given particle can be obtained by fitting $\partial F_\omega/\partial z$ (0, z) (derived from eq A10) with a value of q that describes the observed $\Delta \nu(\omega)$ versus z for the particle. Theoretically, $\partial F_\omega/\partial z$ depends on where the charge sits within the polarizable sphere. There are two extremes, where the charge is concentrated at the top or the bottom of the particle. In Figure 5, these are the upper and lower curves, respectively. The width of this range has an inverse relationship to the particle dielectric constant, ϵ. In these calculations, ϵ is taken to be 10, the bulk value of CdSe.

The range of possible signals from a single charge introduces a source of uncertainty into the calculation of absolute nanoparticle charge. The rate of decay of the upper curve is somewhat faster than that of the lower; theoretically, the data can be fitted with two parameters, q and s, to try to determine the position of the charge within the particle. However, the precision of the data does not allow us to distinguish between the upper and lower curves. Charge migration and blinking that take place on a time scale faster than a $\Delta \nu(\omega, z)$ versus z curve can be obtained (~100 minutes) complicate the analysis, as can be seen from Figure 5c and d showing that the charge signal does not always follow a smoothly decaying trend such as in Figure 5a and b. The quick falloff of the signal with tip–surface separation makes it impossible to obtain decay data for a z range grater than ~20 nm. Small signal amplitudes also do not allow us to distinguish a point charge from a dipole-type signal based on the decay rate of $\Delta \nu(\omega, z)$ with tip–surface separation. At present, this distinction can be made only on the basis of relative signal strengths.

A total of ~7000 nanocrystal charge measurements were analyzed, and the results for 4 experiments are summarized in the histograms shown in Figure 6.[22] Uncharged particles are not included here, but the relationship between the concentrations of charged and uncharged particles is shown in Figures 16–19. The histograms appear to have peaks that occur at integral values of elementary charges. The cumulative distribution can be approximated by a sum of Gaussians around integer multiples of elementary charges. We emphasize that these are not best-fit distributions with arbitrarily placed peaks. Rather, these are curves placed to guide the eye in an attempt to rationalize the observed data physically. The distribution shifts to higher charge states (a) with higher-frequency excitation, (b) on N- rather than on P-type silicon, and (c) on thicker rather than thinner oxides. A kinetic model is discussed in section 5.

Figures 7–10 show cross-sectional line profiles of the types of charge signals observed. Figure 7a shows four charge profiles for the same particle taken at different times during the course of a 17-h experiment. One of the profiles corresponds to a time prior to exposure and shows no charge signal from the particle. A similar profile after a long relaxation period is also shown. Plotted on the same panel are signals that correspond to 1 and 2.7 positive charges, assuming that the charge is at the particle center. Figure 7b shows the data corresponding to one hole at

Photoionization of CdSe/CdS Nanocrystals

*J. Phys. Chem. B, Vol. 108, No. 16, 2004* **4949**
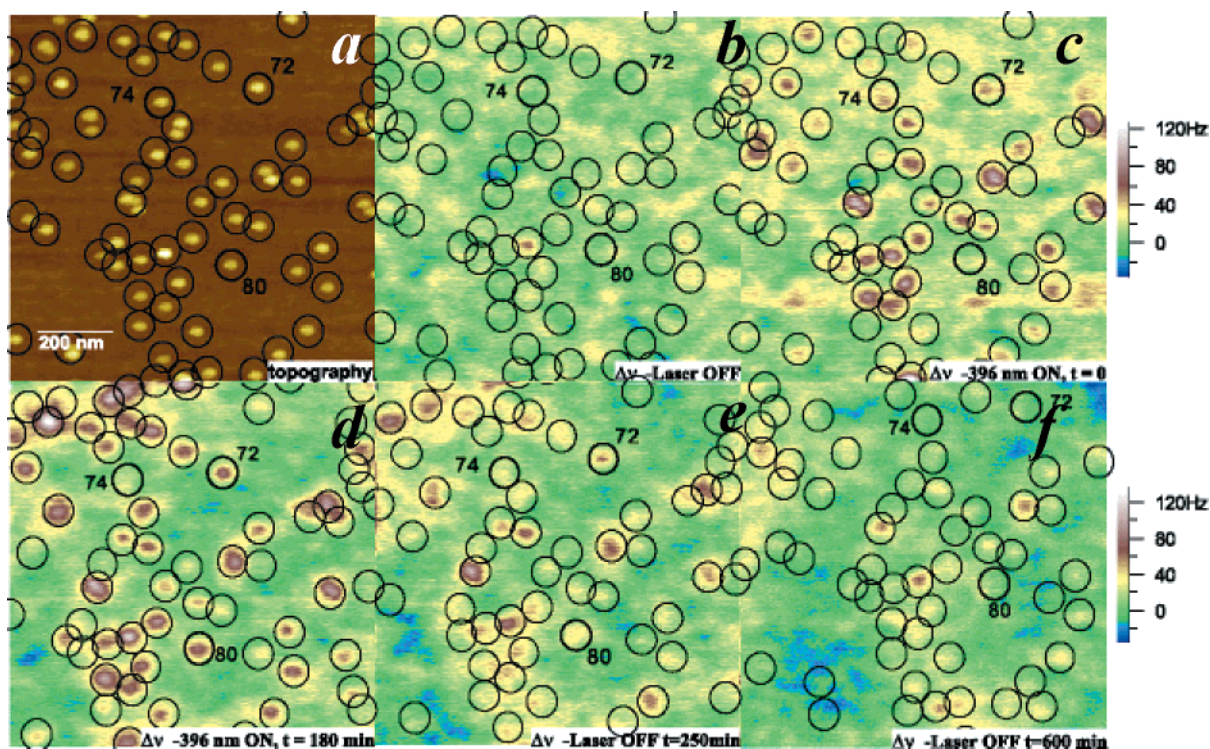
Figure 3. Topography (a) and charge (b−f) images of the same sample area of CdSe/CdS nanocrystals on N-type silicon with 12 Å, exposed to 396-nm photoexcitation. (b) Charge image prior to high-energy excitation; (c) first image taken once the laser is turned on; (d) image taken at t_{on} = 180 min; (e) image taken 250 min after the laser is turned off; (f) t_{off} = 600 min.
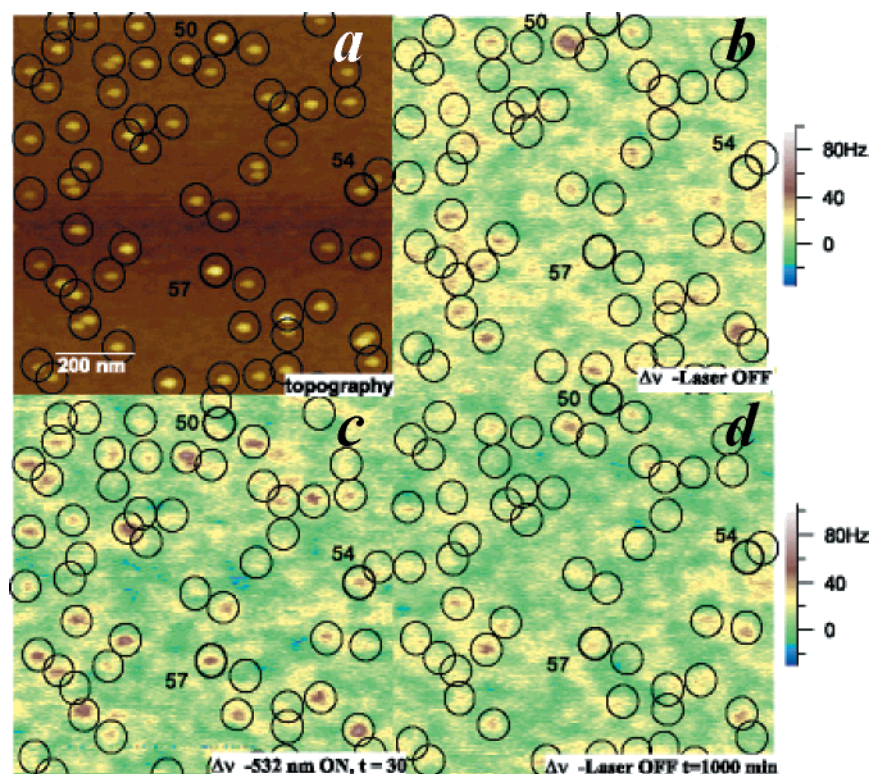
Figure 4. Topography (a) and charge (b−d) images of the same sample area of CdSe/CdS nanocrystals on P-type silicon with 12 Å, exposed to 532-nm photoexcitation. (b) Charge image prior to high-energy excitation; (c) image taken at t_{on} = 30 min; (d) t_{off} = 600 min.

the center of a nanoparticle superimposed onto calculated force gradients for a particle with the same diameter. Three calculated curves are shown; the bottom and top dashed curves are for the charge at the bottom and the top of the particle, respectively, and the solid curve in the middle corresponds to a charge at the center. The experimental curve agrees well in magnitude

and width with the calculated one for the charge located in the center.

The baseline around the particle in Figure 7 is relatively flat and does not show any serious irregularities. However, the baseline in Figure 8 shows a strong dip on the right side of the particle. This kind of a dip may be associated with an underlying
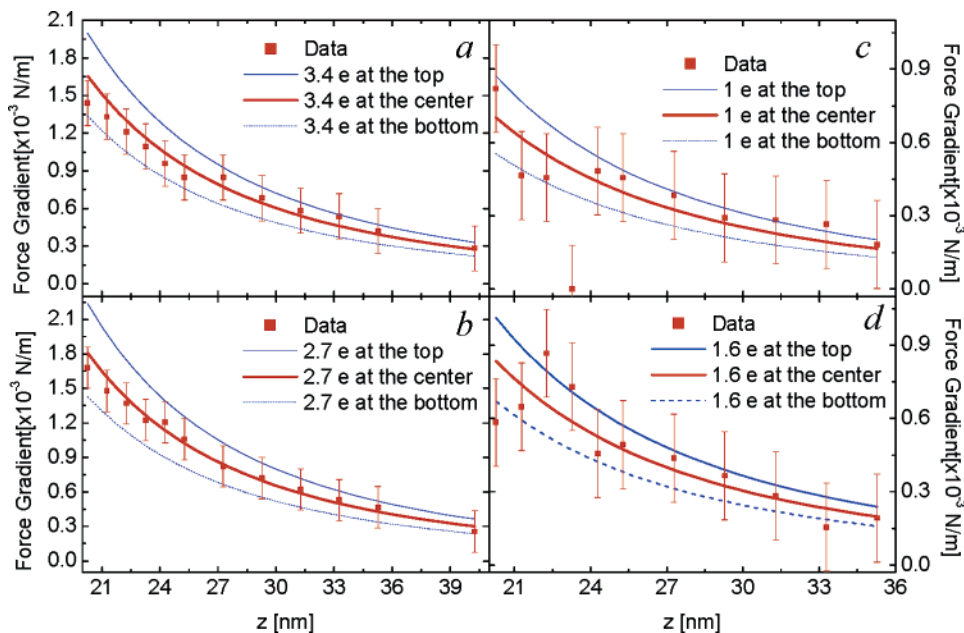
Figure 5. Upper and lower curves in each panel are the calculated signal strengths for a point charge of specified magnitude at the top and bottom of the particle, respectively. The middle curves show the best fit of $\partial F_\omega(z)/\partial z$ vs z for particles with calculated charges of 3.4e (a), 2.7e (b), 1e (c), and 1.6e (d) concentrated at the center of the particles.
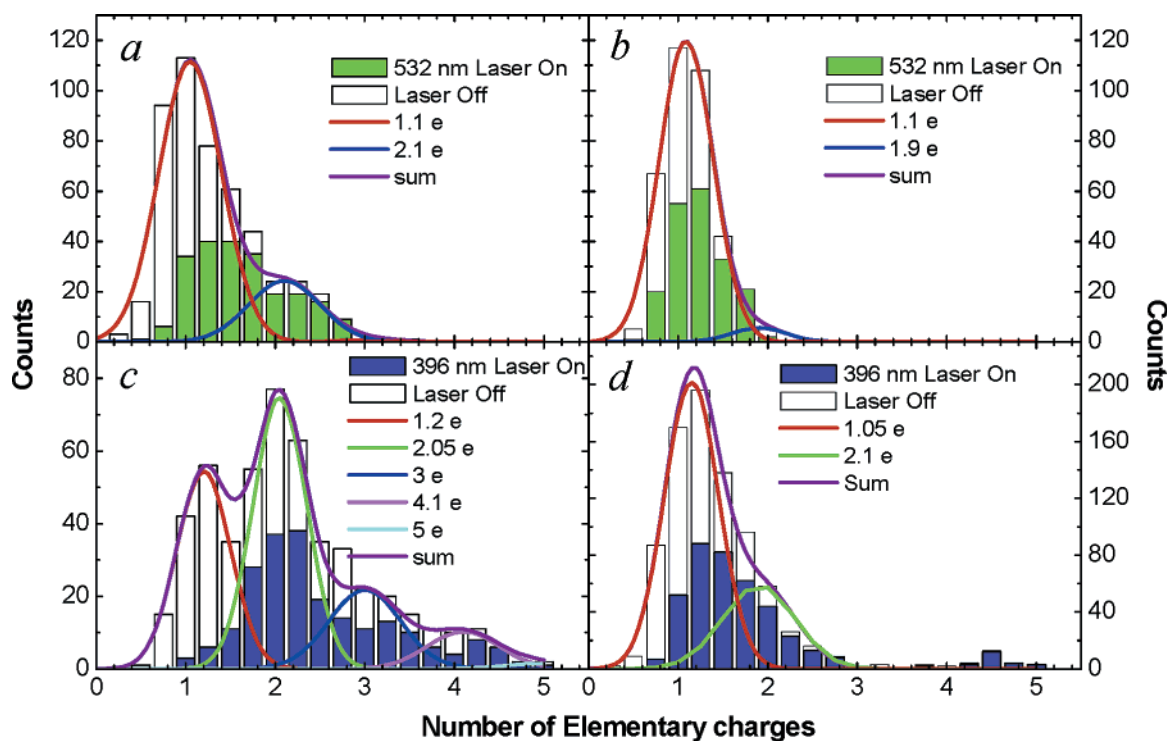
Figure 6. Histograms of charge counts observed during the course of photoexcitation experiments on N-type silicon with 14-Å SiO_2 and 532-nm excitation (a), P-type silicon with 14-Å SiO_2 and 532-nm excitation (b), N-type silicon with 21-Å SiO_2 and 396-nm excitation (c), and P-type silicon with 21-Å SiO_2 and 396-nm excitation (d). The shaded area of the histogram corresponds to the counts collected during photoexcitation (laser on), and the unshaded areas correspond to relaxation periods. The solid curves labeled "sum" are cumulative distributions obtained by summing over Gaussian peaks with means indicated in each panel. These curves are not best multipeak Gaussian fits but are included to show that the distributions can be due to species with multiple elementary charges.

negative charge in the SiO_2 or a local work function variation in this N-type silicon substrate. The baseline irregularity introduces additional error in determining the particle charge. Panel b of the same figure shows the range of calculated charge profiles for a particle with three positive charges superimposed onto two experimental line scans, corresponding to 3 and 2.5 positive charges at the center. The width and magnitude of the signal corresponding to 2.5 charges agree well with the

calculated curve for 3 positive charges at the bottom of the particle.

The particles in Figures 7 and 8 show line widths consistent with the calculations over the whole time span of the experiment. The particle in Figure 9, however, shows significant broadening of the charge signal over time. In panel a, the particle starts in a neutral state and becomes charged upon photoexcitation. Initially, the charge signal is narrow and agrees with the

Photoionization of CdSe/CdS Nanocrystals

*J. Phys. Chem. B, Vol. 108, No. 16, 2004* **4951**
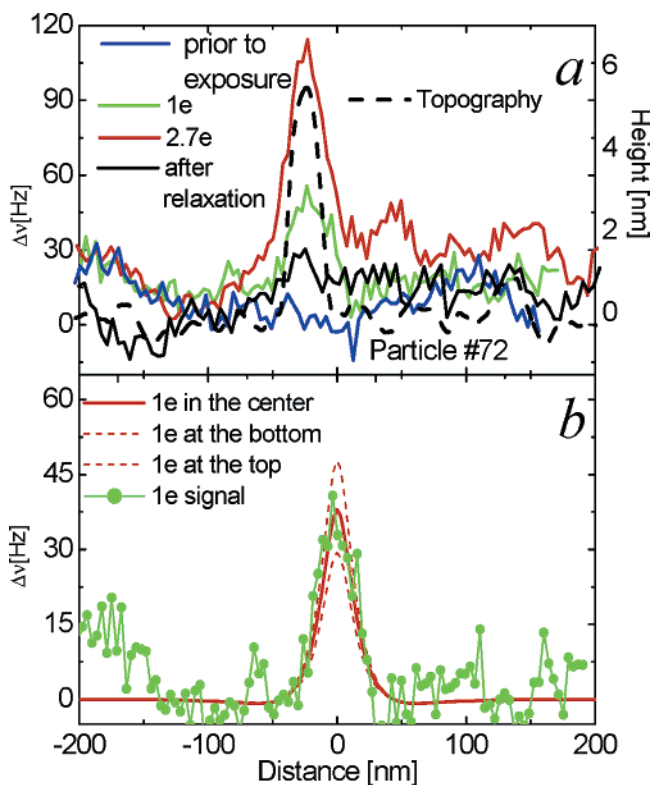
Figure 7. (a) Topographic line scan and several charge profiles for the same CdSe/CdS particle on N-type Si with 14-Å SiO$_2$ and 396-nm excitation at several different times during the experiment: uncharged, before exposure; shortly after exposure showing a charge of 1 e; later, showing a charge of 2.7 e; and after complete relaxation. (b) Superposition of a measured signal corresponding to 1e at the center of the particle and three calculated charge profiles for the bottom 1e at the top, center, and bottom of the particle.

Figure 8. (a) Topographic line scan of several charge profiles for the same CdSe/CdS particle on N-type Si with 21-Å SiO$_2$ and 396-nm excitation at several different times during the experiment: uncharged, before exposure; after relaxation; and during exposure showing charges of 2 e, 2.6 e, and the highest observed signal for this particle of 3.8 e. (b) Superposition of measured signals corresponding to 3 and 2.5e at the center of the particle and three calculated charge profiles for 3e at the top, center, and bottom of the particle. The 2.5e agrees well with the calculation for 3e at the bottom of the particle.

calculations (Figure 9b). After some time, the signal becomes much broader than predicted for a particle of this size (Figure 9c). Under the current model, this type of broadening cannot be explained by any charge distribution within the particle. We interpret it to be due to charge buildup in the oxide underneath the particle. Charges that are further away from the probe appear broader in the EFM images.

The particle in Figure 9 is part of the experiment on N-type silicon with 21-Å SiO$_2$, photoexcited with 396-nm light. Control experiments on clean substrates showed that charge buildup in the oxide can occur in certain areas of the N-type substrates with thicker oxides when photoexcited at 396 nm. Figure 10 shows topography and charge images corresponding to 160 min of photoexposure to 396 nm of N-type silicon with 21-Å SiO$_2$. The charges on the sample that do not correspond to particles are marked by red squares. There are several such charges on this sample, but none are seen in the experiment in Figure 3 for the same conditions on a 14-Å-thick SiO$_2$ layer, most likely because the holes trapped close to the Si/SiO$_2$ interface tunnel back on short time scales. P-type substrates also did not show such charge buildup, nor did 532-nm light produce any appreciable oxide charging, most likely because of the substantially lower absorption coefficient of the silicon at low frequencies ($\alpha_{Si}(532) = 6.55 \times 10^3$, $\alpha_{Si}(396) = 8.98 \times 10^4$) and shorter tunneling lengths for lower-energy carriers.

All of the charge profiles discussed so far were for particles on N-type substrates. Figure 11 shows line profiles for two different particles on a P-type substrate with 21-Å SiO$_2$ excited at 396 nm. As seen in Figure 6b and d, most particles on P-type substrates have one or two charges such as in the line profile in

Figure 11a. Also, from Figure 4 we can see that on P-type substrates there is some charging of the particles even prior to photoexcitation. It is possible that there is stronger communication between the particles and the P-type substrate that does not involve the 396-nm laser light. In fact, the kinetics analysis shows that during the relaxation (in the dark) both the forward and back electron-transfer rates are faster on P-type than on N-type substrates.

In addition to small (1−2 e) signals commonly seen on P-type substrates, a single outlier behavior was observed in a particle showing up to 5 positive charges, with no line broadening (Figure 11b−d). This particle started with a nonzero charge before excitation and returned to approximately the same state after relaxation. The superposition of calculated and experimental curves (Figure 11c and d) confirms that the line widths of the charge signal due to this particle agree with theoretical predictions.

B. Individual Particle Charge versus Time Traces. Figures 12−15 show a number of single-particle "charge versus time" traces that demonstrate general trends as well as the diversity of observed behavior.

Experiments on 14- and 21-Å-thick oxides on P-type substrates are shown in Figures 12 and 13. The solid green squares show the charge state during 532-nm excitation, and the purple circles represent the data during 396-nm photoexcitation for the same particle. The hollow symbols represent the subsequent relaxation. The charge state was set to zero if the signal was
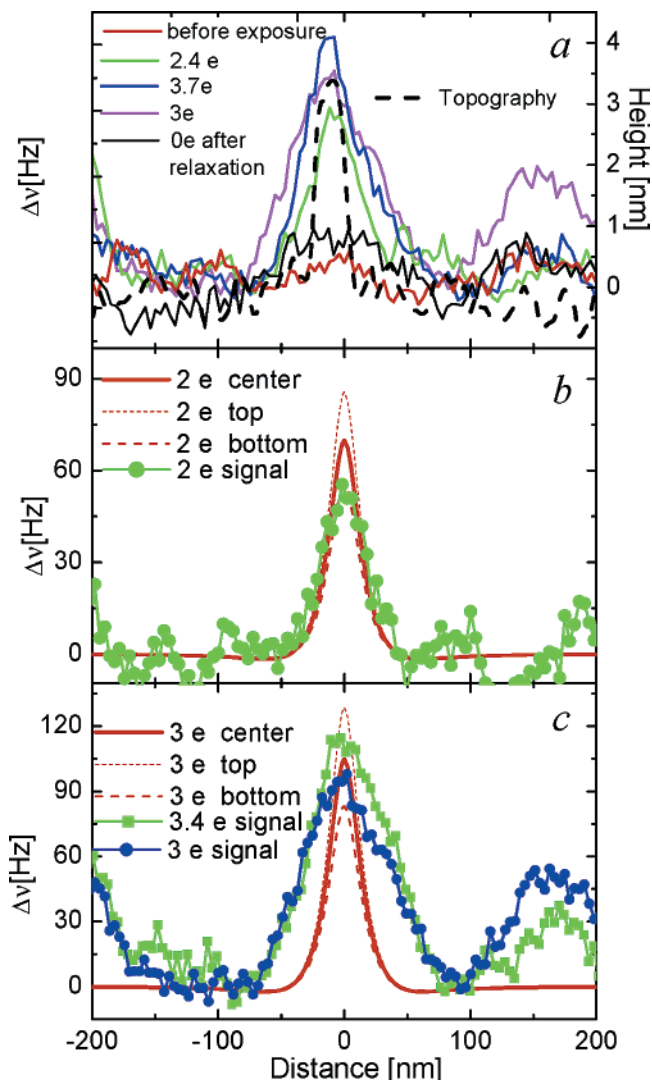
Figure 9. (a) Topographic line scan of several charge profiles for the same CdSe/CdS particle on N-type Si with 21-Å SiO$_2$ and 396-nm excitation at several different times during the experiment: uncharged, before exposure, and after relaxation; during exposure showing charges of 2.4, 3.7, and 3e. The signal shows line broadening with time. (b) Superposition of measured signals corresponding to 2e at the center of the particle and three calculated charge profiles for 2e at the top, center, and bottom of the particle. (c) Line broadening of the signal. The calculated curves are not at all representative of the observed line widths for the two signals shown.
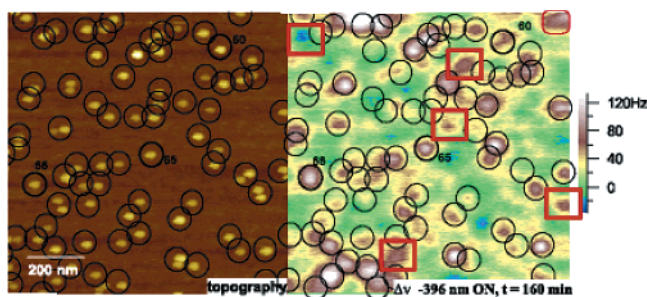
Figure 10. Topography and charge images of a nanoparticle sample on an N-type silicon substrate with 21-Å SiO$_2$ exposed to 396-nm radiation. The red squares in the charge image indicate charged islands that do not correspond to nanocrystals on the surface.

indistinguishable from the baseline noise, represented by the shaded area around the time axis.

Panels a and b of Figure 12 are representative of P-type silicon with 14-Å SiO$_2$; similar behavior was seen from most particles

with 532- and 396-nm excitation. Some particles showed higher charge at 396 nm (Figure 12a), some showed higher charge at 532 nm (Figure 12b), but others were almost indistinguishable at the two wavelengths. Figure 12c shows a particle that was much more intermittently charged than the other two.

The majority of the 10 particles analyzed on P-type silicon with 21-Å SiO$_2$ acquired more charge when photoexcited at 396 nm. An extreme example is shown in Figure 13a, where the particle acquired up to 5 charges. (Line profiles for both particles in a and b are shown in Figure 11.) However, equivalent responses at the two wavelengths were also observed (Figure 13c). In addition, some particles showed almost no response at 532 but did charge at 396 (Figure 13d). In general, it is apparent that the behavior on P-type substrates is marked by discrete jumps and on/off intermittency with charge magnitudes very rarely exceeding two holes per particle.

Figure 14 shows the time traces for the 396- and 532-nm photoexcitation experiments for N-type substrates with 14-Å SiO$_2$ layers. Part a of Figure a shows one of the larger signals observed for this experiment, part b is more representative of the 10 individually analyzed particles, and part c shows a particle with less charge and a higher degree of intermittency than is common on this substrate. With 532-nm excitation (Figure 14d−f), the particles show on average less charge than with 396-nm light (Figure 14a−c).

The particle in Figure 14d appears to make a gradual transition from 1 to 2 elementary positive charges, and when the laser is turned off, it decays through one apparent intermediate point to a singly ionized state. By contrast, the particle in panel e appears to reach equilibrium immediately. However, when the laser is turned off, it relaxes very gradually, going through a large number of intermediate steps. Part f of Figure 14 shows a particle that behaves like the particle in part c of Figure 14, showing a lot of intermittency and presenting at most a single charge.

Charge versus time traces on N-type substrates with thicker, 21-Å oxide layers are shown in Figure 15. Comparison with Figure 14 shows that the decay rates in the dark are much slower on the thicker oxides. Full relaxation curves were obtained only for the 396-nm excitation experiment on these substrates. However, the data on the thinner oxides for both N- and P-type silicon show that relaxation in the dark is independent of the initial photoexcitation wavelength. Once again, a range of behaviors was observed, with the maximum charge per particle reaching between 1 and 5 elementary positive charges. On average, more strongly charged particles were observed on the thicker oxides for both 532- and 396-nm excitation. Gradual relaxation behavior (Figure 15b) was predominant, yet discrete jumps (Figure 15a) were also seen.

5. Heuristic Ensemble Kinetic Model

A four-parameter model was necessary to analyze the trends in the particle photoionization kinetics quantitatively under different experimental conditions. The particles are assumed to transfer between subsequent ionization states according to

$$|0\rangle \underset{k_b}{\overset{k_f}{\rightleftharpoons}} |+1\rangle \underset{ak_b}{\overset{k_f/a}{\rightleftharpoons}} |+2\rangle \underset{a^2 k_b}{\overset{k_f/a^2}{\rightleftharpoons}} |+3\rangle \cdots \underset{a^{n-1}k_b}{\overset{k_f/a^{n-1}}{\rightleftharpoons}} |+n\rangle \quad (8)$$

There are two rates k_f and k_b for initial photoionization. For each subsequent electron-transfer step, the previous forward rate is divided by a factor of a, and the back-transfer rate is scaled by this factor. A large a implies a slower second-ionization step. The physical meaning of a will be described later.

Photoionization of CdSe/CdS Nanocrystals

*J. Phys. Chem. B, Vol. 108, No. 16, 2004* **4953**
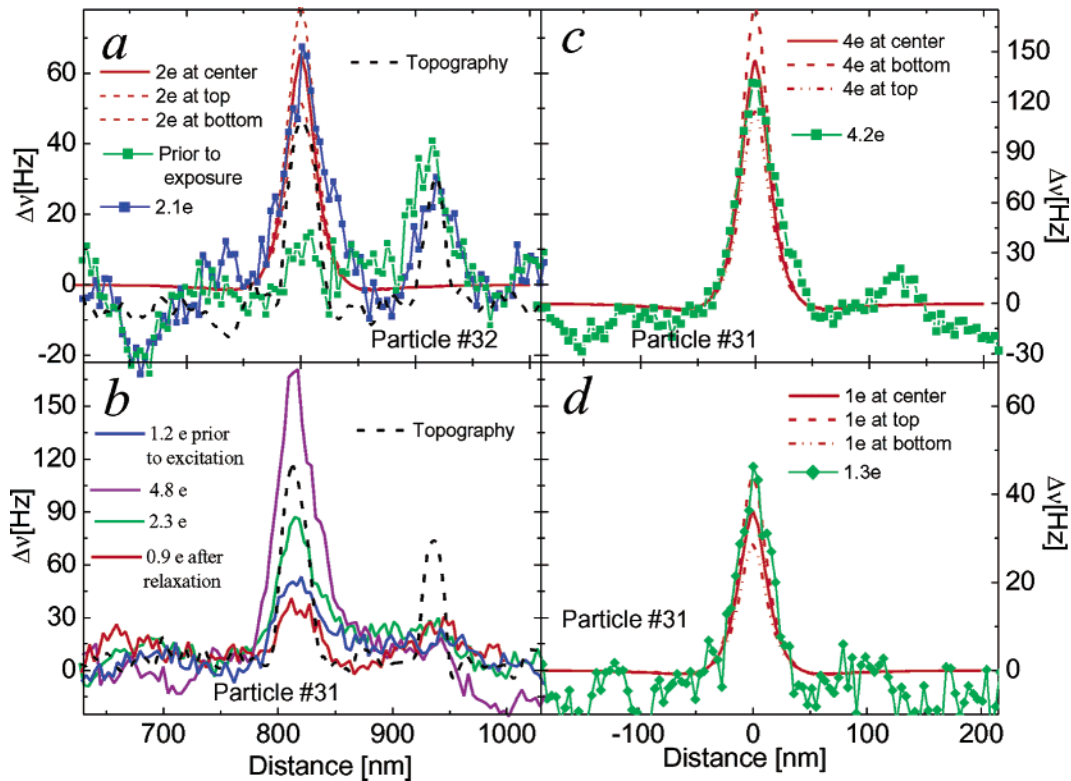
Figure 11. (a) Superposition of calculated charge profiles and two observed charge profiles for the same CdSe/CdS particle on P-type Si with 21-Å SiO_2 exposed to 396-nm light: uncharged prior to excitation and charged with 2.1e after being exposed. The signal shows line broadening with time. (b–d) Charge profiles for another particle in the same experiment that has uncharacteristically high charge. (c) Superposition of the 4.2e signal onto calculated charge profiles for a particle containing 4e and the (d) 1.3e signal onto calculated profiles for 1e on a particle. The 4.2e signal agrees well with a charge at the particle center, and the 1.3e signal is well described by a single electron at the top of the particle.

The relative time-dependent concentrations of $|+n\rangle(t)$ are governed by a system of coupled first-order differential equations

$$\frac{d}{dt}\begin{pmatrix} |0\rangle \\ |+1\rangle \\ |+2\rangle \\ |+3\rangle \\ \vdots \\ |+n-1\rangle \\ |+n\rangle \end{pmatrix} =$$

$$\begin{pmatrix} -k_1 & k_2 & 0 & & 0 & 0 & & 0 \\ k_1 & -\left(\frac{k_1}{a}-k_2\right) & ak_2 & & 0 & \vdots & & \vdots \\ 0 & \frac{k_1}{a} & -\left(\frac{k_1}{a^2}-ak_2\right) & \vdots & 0 & & & \vdots \\ \vdots & 0 & \frac{k_1}{a^2} & & \vdots & a^{n-3}k_2 & & 0 \\ \vdots & \vdots & 0 & & \vdots & -\left(\frac{k_1}{a^{n-2}}-a^{n-3}k_2\right) & a^{n-2}k_2 \\ 0 & 0 & 0 & & 0 & \frac{k_1}{a^{n-2}} & & a^{n-2}k_2 \end{pmatrix} \begin{pmatrix} |0\rangle \\ |+1\rangle \\ |+2\rangle \\ |+3\rangle \\ \vdots \\ |+n-1\rangle \\ |+n\rangle \end{pmatrix}$$

(9)

which can be solved as an eigenvalue problem for an arbitrary value of n and an initial conditions vector α.

The data set subjected to this analysis was constructed in the following way: Throughout the experiment, we followed a fixed field of view of ~100 particles. At any time, this field was composed of two groups: charged and uncharged. Some particles (a) were "active" and had a high probability of being charged, and others (b) were inactive and essentially never

charged. For 10 particles from group (a), the exact charge state was measured at every point in time. The number of uncharged particles was also recorded. We assumed that the 10 particles were representative of group (a). A particle was counted as being in state $|+n\rangle(t)$ if its calculated charge q at time t satisfied $n - 0.5 \leq q < n + 0.5$. In this way, the counts for $|+n\rangle(t)$ for $n = 1,...,6$ were recorded. The counts of $|+n\rangle$ were normalized and scaled by the fraction of all of the particles that were charged in the given sample at that time t, which determined their concentrations relative to $|0\rangle$. The error bars on these counts were determined from simulating the counting process with a random Gaussian error[23] with a mean of 0 and a standard deviation of 0.6e representing the different charge locations and instrument noise.

The counts of uncharged particles did not reflect how many of these were active and how many were inactive because observing an uncharged particle at all times $t < T$ does not preclude it from becoming active at time $T + 1$. Hence, another fitting parameter, the fraction of active particles f, was introduced to determine how many particles are in group (a): $f = a/(a + b)$. Because all of the particles in group b are always in state $|0\rangle$, f was introduced through the initial conditions vector $\alpha = [f_1|0\rangle(0), |+1\rangle(0),..., |+n\rangle(0)]$, and $f_1 = (f - \sum_{i=1}^{n}|+i\rangle(t = 0))/|0\rangle(t = 0)$. Without this parameter, the model did not describe the data.

A substantial fraction of particles in most of the experiments never became charged (group (b)), which suggests that these particles have a structural defect that causes ultrafast exciton recombination or that the charging/discharging cycle is faster than can be detected by our setup. Yet, as we show below, the fraction of active particles was larger on the thinner oxide; this suggests that the local oxide properties also influence charging.
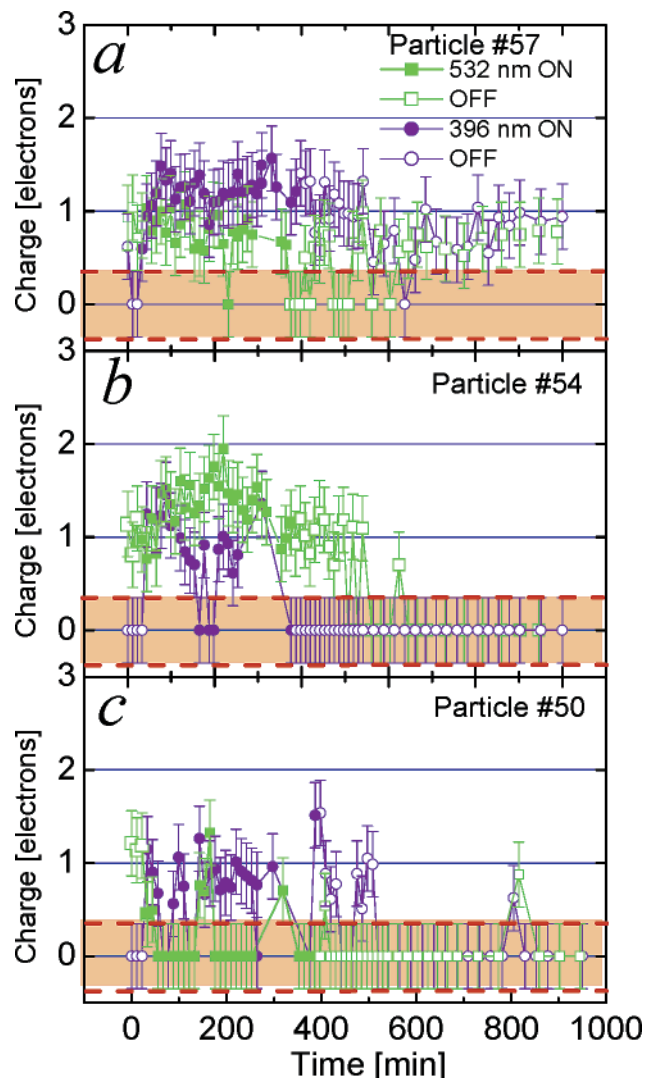
Figure 12. Charge vs time traces for three different particles on P-type silicon substrates with 14-Å SiO$_2$. In each panel, filled purple circles and green squares correspond to 396- and 532-nm photoexposure times for the same particle. The unshaded symbols correspond to subsequent relaxation. The points whose signal strength was below the noise level, indicated by the shaded area around the charge = 0 axis, were assigned a value of zero. (a) A particle that was more highly charged when exposed to 396-nm light; (b) a particle that was more responsive to 532 nm; (c) a particle that was much more intermittently charged than the other two.

Results of Model Fitting. Modeling results for four out of eight experiments are shown in Figures 16−19: the points represent the normalized counts, and the solid lines, the model fits. Panel *a* of each figure shows the rise-time kinetics for the photoionization process (laser on), and panel *b* shows the relaxation (laser off). The values of the forward and back electron-transfer rate constants as well as *a* are allowed to vary for photoionization and relaxation, but *f* is kept the same. The best-fit parameters for all experiments are summarized in Table 1.

The model describes the experiments on P-type substrates with 396-nm excitation for 21- and 14-Å SiO$_2$ quite well (Figures 16 and 17). A lot more charging is observed on the thicker oxide. During the excitation, the forward rate from the nanocrystal excited state is similar for both experiments. The backward rate to the ionized nanocrystal on the thinner oxide is faster, resulting in the skewing of the equilibrium concentrations toward zero charge.

Figures 18 and 19 show the model fits and experimental data for N-type substrates with 14-Å SiO$_2$ for 532- and 396-nm excitations, respectively. Much larger concentrations of multiply charged particles and much slower relaxation rates for the particles on N- compared to P-type substrates are observed. We previously postulated that this is due to the faster back-transfer rates on P-type silicon, which result from an increased number of electrons held near the surface because of band bending induced by dangling bond states.[14] On N-type silicon, the bands bend in the opposite direction, which causes a depletion of mobile electrons at the surface, causing slower back-transfer rates with and without photoexcitaion. The silicon substrates used in this set of experiments were forming gas annealed to remove some of the dangling bond defects. However, the work function difference we measured by EFM, between these degenerately doped N- and P-type substrates, was ∼0.55 V instead of the 1 V expected for flat-band silicon with complete interface passivation.[24] Thus, a large degree of band bending still remained.

If we compare the relative back and forward electron-transfer rates (k_b/k_f) for the corresponding experiments on N- and P-type substrates, we notice that the ratio is always greater on P-type silicon. Unfortunately, we cannot directly compare the rate constants themselves because they should be functions of the excitation intensity, which is not constant from experiment to experiment because of the diffuse grazing-angle excitation of the sample. We can, however, compare back-transfer rates in the dark, which are always greater on P-type silicon. In fact, the effect of band bending on the back transfer rates in the dark is *much* stronger than that of the thickness of the tunneling barrier. The forward rates also appear to be much larger in the dark on the P- than on the N-type substrates, which may be due to fast electron exchange with the ionized (positive) donors at the P-type Si−SiO$_2$ interface.

If the rates are determined by direct tunneling, then the rate constants can be approximated by

$$k_{f,n+1} \propto e^{-2\sqrt{2m(V_0 + \Delta E_{n+1} - E_\lambda)}(l/\hbar)} \quad (10)$$

which represents the tunneling of an electron with energy E_λ through a barrier of physical thickness l and height $V_0 + \Delta E_{n+1}$. ΔE_{n+1} represents the energy necessary to put an $(n+1)$ electron onto a capacitor, here defined by the spherical particle and a conductive plane:

$$\Delta E_{n+1} = {}^1\!/_2(2n+1)\frac{e^2}{C_{particle-plate}}$$

where $e = 1.6 \times 10^{-19}$ C and $C_{sphere-plate}$ is given by eq A2. For a particle−substrate separation of 21 Å, $\Delta E_{n+1} \approx 0.31(2n + 1)$ eV, and $\Delta E_{n+1} \approx 0.29(2n + 1)$ eV for 14 Å. If we Taylor expand the square root of the exponent to first order in ΔE_{n+1}, then we get

$$k_{f,n+1} \approx e^{-2\sqrt{2m(V_0 - E_\lambda)}(l/\hbar)} \times e^{-\frac{l\sqrt{2m}}{2\hbar\sqrt{(V_0 - E_\lambda)}}\frac{(2n+1)e^2}{C_{s-p}}} \approx$$

$$k_{f,1}\left(e^{-\frac{l\sqrt{2m}}{\hbar\sqrt{(V_0 - E_\lambda)}}\frac{e^2}{C_{s-p}}}\right)^n \quad (11)$$

Physically, fitting parameter *a* should capture the increasing

Photoionization of CdSe/CdS Nanocrystals

J. Phys. Chem. B, Vol. 108, No. 16, 2004 **4955**
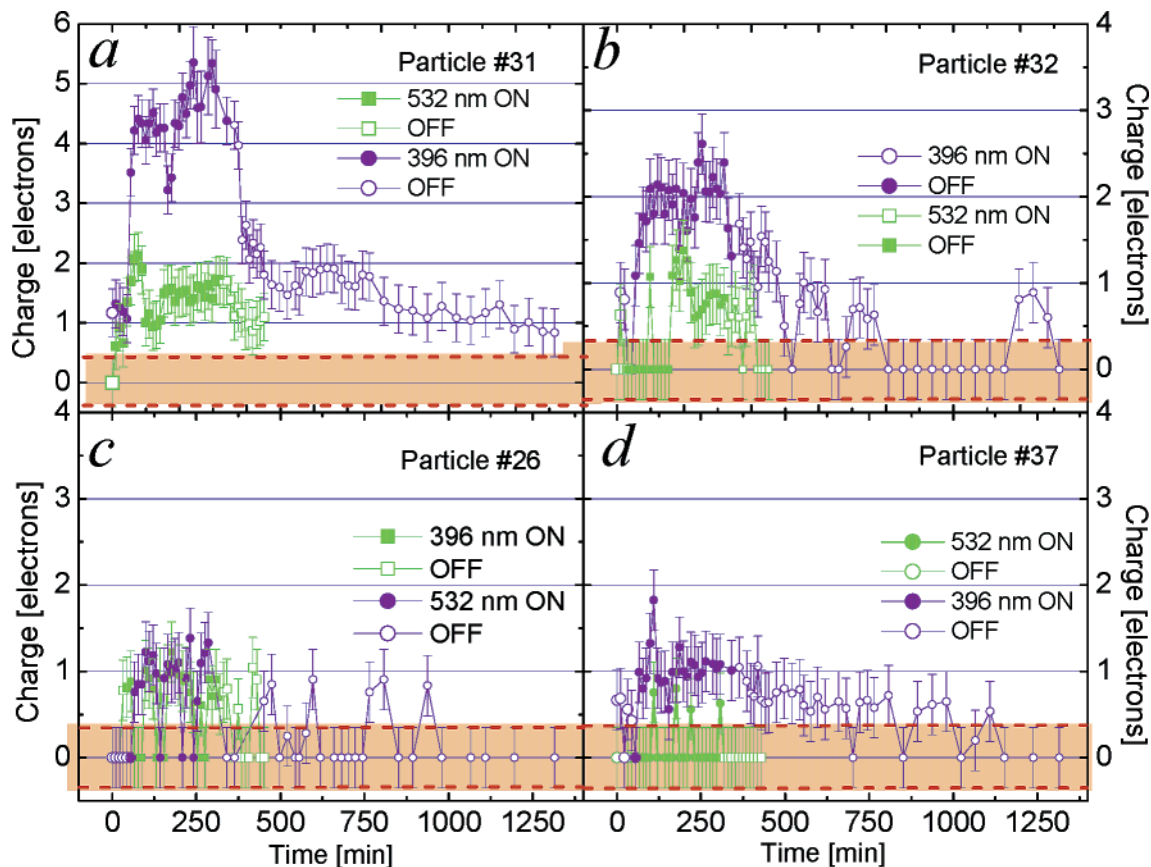
Figure 13. Charge vs time traces for four different particles on P-type silicon substrates with 21-Å SiO_2 to demonstrate the wide range of observed behavior. The legend is as described for Figure 4.10. (a) Outlier particle that was much more highly charged than any other particle on the P-type substrate and showed slower relaxation dynamics; (b) representative behavior for particles on this substrate, with more charging when exposed to 396-nm light; (c) a particle with a highly intermittent charge state oscillating around 1e; and (d) a particle that was mostly uncharged with 532- and had a low charge with 396-nm excitation.

ionization energy with each additional charge,

$$a \approx e^{\frac{l\sqrt{2m}}{\hbar\sqrt{(V_0 - E_\lambda)}}} \frac{e^2}{C_{s-p}} \qquad (12)$$

By analogous reasoning, the inverse back-transfer rate relationship can be obtained. This a^n dependence of the rates is a good approximation only for small values of n. Because ΔE grows quickly with n, using only the first term of the Taylor series overestimates a. Figure 20 shows the relative band offsets of the CdSe particle[25] with respect to Si and SiO_2 band levels. With reference to the Si valence band (VB), the tunneling barrier V_0 for SiO_2 is ~4.3 eV; the energy of the electron excited from the CdSe VB at 532 nm is ~2 eV and ~2.8 eV for an electron excited at 396 nm. The effective mass of the electron tunneling through SiO_2 is ~$0.34m_e$.[26] If we calculate a as described by eq 12, then we get the following values for $a_{i,j}$ (2.2, 2.7, 3.7, 4.9), where $i = 14$ or 21 Å and $j = 532$ or 396 nm. If we calculate the average k_{n+1}/k_n for the first five rate constants using eq 10, then we get somewhat smaller values: (2, 2.2, 3, 3.6). Looking at the fitting results for a in Table 1, we can see that these numbers are well within an order of magnitude of the observed behavior.

We can estimate tunneling rates

$$k^\lambda_{tunnel} = \frac{k_f}{N_\lambda} \frac{1}{\tau_\lambda}$$

where k_f is the observed forward electron-transfer rate given in Table 1, $N_\lambda = I\sigma_\lambda\lambda/hc$ is the number of optical excitation per

second ($\sigma_{532} = 5.2 \times 10^{-16}$ cm² and $\sigma_{396} = 2.3 \times 10^{-15}$ cm²), and τ_λ is the lifetime of the particle excited state. $\tau_{532} \approx 150$ ps and $\tau_{396} \approx 1$ ps for ensemble measurements;[27,28] the 532-nm value, controlled by energy transfer into the substrate, is taken from an estimate on an Au substrate. These are order-of-magnitude values; the lifetimes of individual particles at room temperature differ by orders of magnitude and fluctuate in time.[29] The tunneling rates and per-excitation tunneling probabilities are given in Table 2.

Using eq 10 and parameters for electron tunneling through SiO_2 given above, the tunneling rates at the same excitation wavelength are expected to be at least 2 to 3 orders of magnitude larger on the thinner oxides. But this is not the case for the observed tunneling rates shown in Table 2 if we assume in our calculations of k^λ_{tunnel} that excitation intensity and excited-state lifetimes are the same on all substrates. Energy transfer between chromophores and semiconductors should significantly shorten the excited-state lifetime of the 1S state. The energy-transfer rate has a dependence of between d^{-3} and d^{-4}, where d is the separation of the chromophore and an indirect gap semiconductor.[30] In part, the low observed difference between tunneling rates on thinner and thicker oxides may be from a shorter excited-state lifetime because of more efficient energy transfer between the particles and silicon with the thinner oxides.

Depending on whether d is calculated with respect to the center (~45 and 37 Å) or edge (~20 and 14 Å) of the particle, this effect would give us a factor of between 2 and 5 larger k^λ_{tunnel} on thinner oxides, which is not enough to explain all of
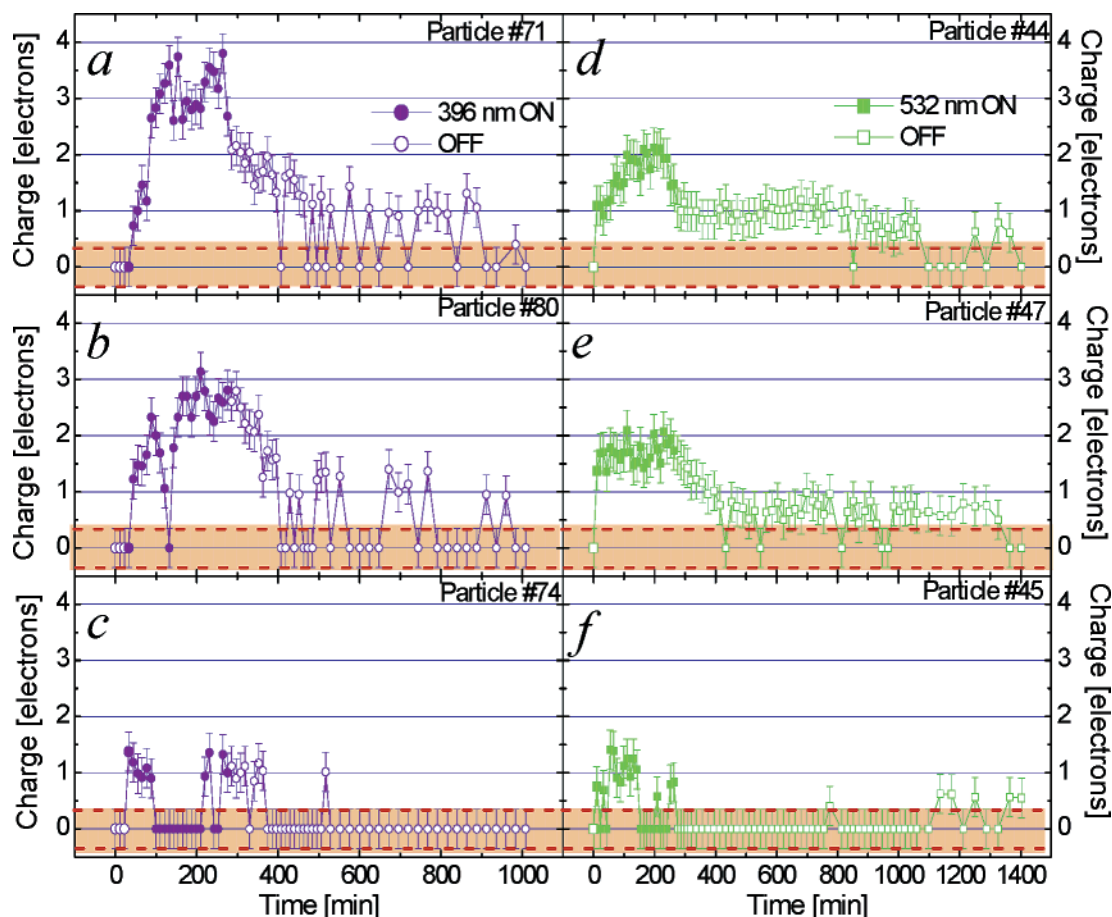
Figure 14. (a−c) Kinetics of photoionization and subsequent relaxation corresponding to 396-nm and (d−f) to 532-nm excitation for six different particles on N-type silicon substrates with 14-Å SiO$_2$. The legend is as described for Figure 4.10. (a) A highly charged particle with very slow relaxation dynamics; (b) representative behavior for particles under this set of experimental conditions; (c) a particle with a highly intermittent charge state oscillating around 1e; (d) the particle has a slow charge onset and discrete relaxation; (e) charging is fast and relaxation takes place through many intermediate states; and (f) a low charge signal with high intermittency.

the discrepancy between theory and experiment. We also expect at least a factor of 5 uncertainty in N_λ due to grazing-angle excitation because the laser alignment was changed between the 14- and 21-Å experiments. The absorption cross section of the nanocrystal may also be affected by the proximity to the silicon substrate; whether it is enhanced or suppressed would affect N_λ and the calculated tunneling rates.

We expect some variations in the electronic barrier height between the thick and thin oxides because the thinner one was prepared with 15% NO in an oxidizing gas and has partial S$_3$N$_4$ character, but the thicker one was not. Oxynitrides are being developed as high-*k* materials for gate insulators that are potentially more resistant to leakage currents than pure oxides.[31−33] Depending on the degree of incorporation of nitrogen into the oxide, the tunneling barrier and carrier effective mass decrease, but the dielectric constant and oxide equivalent thickness increase. This introduces a large uncertainty into the value of the parameters used to calculate the transmission probabilities. In general, there is a lack of agreement in the literature on the value of the effective mass and the validity of the effective mass tunneling model for thin oxides.[31,34] Theoretical calculations of tunneling coefficients that account for the microscopic structure of the oxide show that tunneling through defect levels, such as oxygen vacancies, becomes increasingly important in thinner (<20 Å) oxides.[34] Defect tunneling is energy-dependent; it could be fast at 532 nm and slow at 395 nm or vice versa.

The same discrepancy is evident when comparing reneutralization rates in the dark on thinner and thicker oxides. Although faster back-transfer rates (in the dark) $k_{off,b}$, are observed on the thinner oxides, the difference is not nearly as large as predicted by eq 10 (>10^3 depending on the energy of the back-tunneling electrons). However, these numbers are extremely sensitive to oxide thickness and the local density of defects. The local thickness of SiO$_2$ may be responsible for separating the active particles on thicker substrates from inactive ones such that on average a shorter tunneling length is active on the thicker oxides. On average, there is a larger number of active particles on thinner oxides. Additionally, as seen in Table 1, the doping of the silicon has an effect (up to an order of magnitude) on the rate of back electron transfer that is not accounted for in our tunneling model. Equation 10 does not account for the band bending or the nature of the transition region at the Si/SiO$_2$ interface[34,35] and hence is a very crude approximation of the relative tunneling probabilities.

We also observe that the photoionization rates are faster with higher-frequency photoexcitation. This suggests that fast electron transfer is taking place through higher excited states. Accounting for the higher relative densities of final states in the silicon conduction band ($\rho_c \propto \sqrt{E_\lambda - E_g}$)[36] and using eq 10, we find that tunneling at higher energy is expected to be more likely by a factor of ∼50 for a 21-Å barrier but only by a factor of 16 for a 14-Å barrier.

Photoionization of CdSe/CdS Nanocrystals

J. Phys. Chem. B, Vol. 108, No. 16, 2004 **4957**
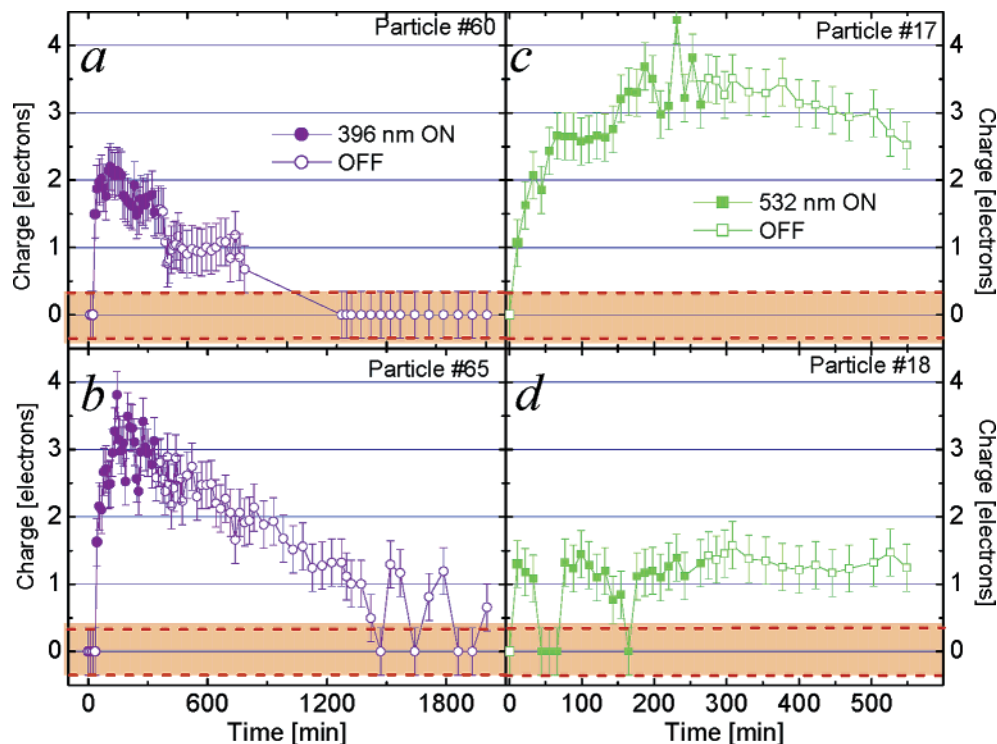
Figure 15. (a, b) Kinetics of photoionization and subsequent relaxation corresponding to 396-nm and (c, d) to 532-nm excitation for four different particles on N-type silicon substrates with 21-Å SiO$_2$. The legend is as described for Figure 4.10. (a) A particle with discrete ionization and relaxation dynamics; (b) a particle that is highly charged and displays continuous relaxation behavior; (c) a representative particle with slow dynamics; and (d) the particle charge signal is low and oscillates around 1e.
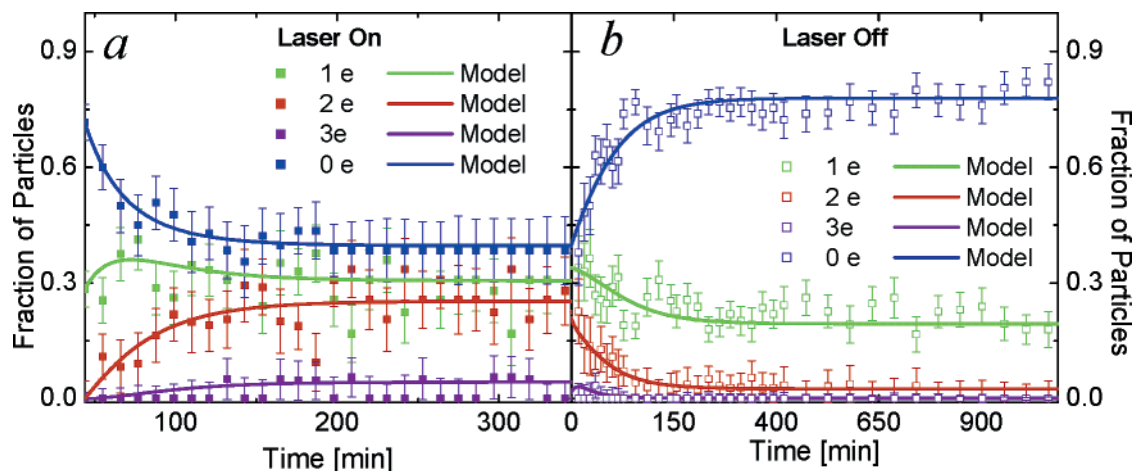
Figure 16. Relative concentrations of particles with 0−3 positive charges as a function of (a) excitation time (396-nm laser on) and (b) relaxation time (laser off) for a sample of nanocrystals on P-type silicon with 21-Å SiO$_2$. The solid curves are fits of a kinetic model described in section 4.4 with corresponding parameters shown in Table 4.1.

The observed ratios of tunneling rates (Table 2) are larger than expected by factors of ∼30 and 6 for the 14- and 21-Å tunneling barriers, respectively. These ratios increase exponentially with *l* so that ratios of ∼250 for a 30-Å tunneling barrier and ∼1300 for a 40-Å barrier are expected. TOPO and CdS layers are also likely to contribute to the tunneling barriers. Hence, we can expect the observed ratios to be somewhat higher than predicted for the 14- and 21-Å barriers. The ratios are consistently larger for the thinner oxides, which also contradicts the predicted trend described above. This observation is consistent with a mechanism involving tunneling through defect states. The width of the tunneling resonance broadens as the oxide gets thinner,[34] and hence it is more likely that a higher-energy electron overlaps with one of these resonances on thinner than on thicker oxides.

Limitations of the Model. Looking at Figures 16−19, we notice that the model is limited in its predictive value. First, the noise in the data, especially evident in Figure 19, suggests that in addition to instrument uncertainty individual particles are not very representative of the ensemble, and a large number need to be analyzed to get a reasonable estimate of average behavior. Also, it is noticeable that this model is much better at describing systems where a lower degree of multiple charging is observed. This again suggests that particles that lose many electrons are probably following slightly different kinetics from the particles that are only singly or doubly ionized and that parameters *a* and *f* are not enough to capture this difference.

The analysis of the fitted rate constants in light of a simple 1D tunneling model is very limited because we do not have
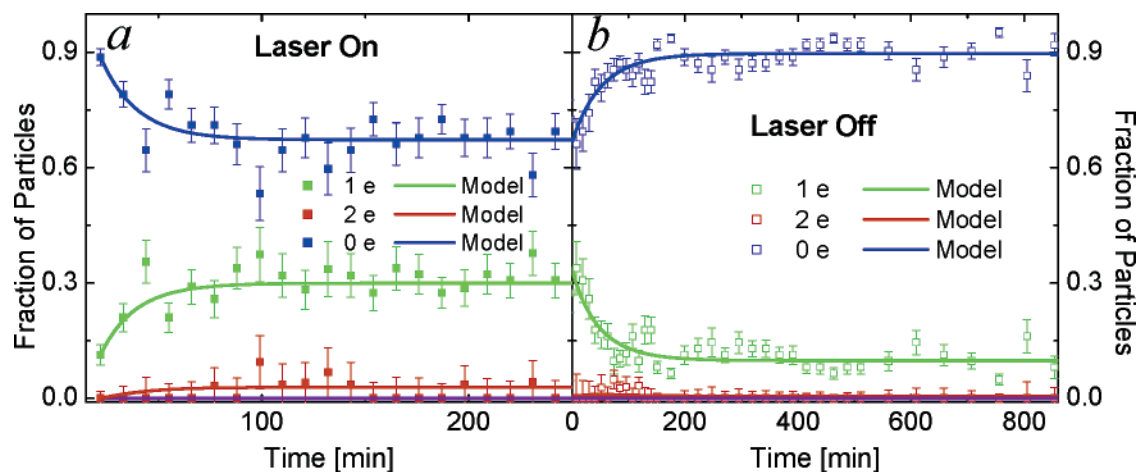
Figure 17. Relative concentrations of particles with 0−2 positive charges as a function of (a) excitation time (396-nm laser on) and (b) relaxation time (laser off) for a sample of nanocrystals on P-type silicon with 14-Å SiO$_2$. The solid curves are fits of a kinetic model described in section 4.4 with corresponding parameters shown in Table 4.1.
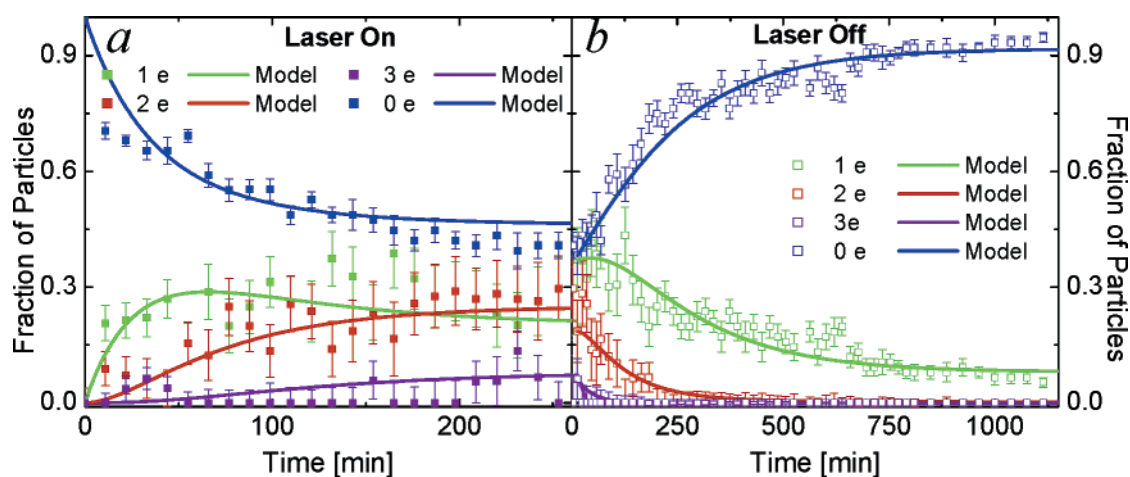

Figure 18. Relative concentrations of particles with 0−3 positive charges as a function of (a) excitation time (532-nm laser on) and (b) relaxation time (laser off) for a sample of nanocrystals on N-type silicon with 14-Å SiO$_2$. The solid curves are fits of a kinetic model described in section 4.4 with corresponding parameters shown in Table 4.1.
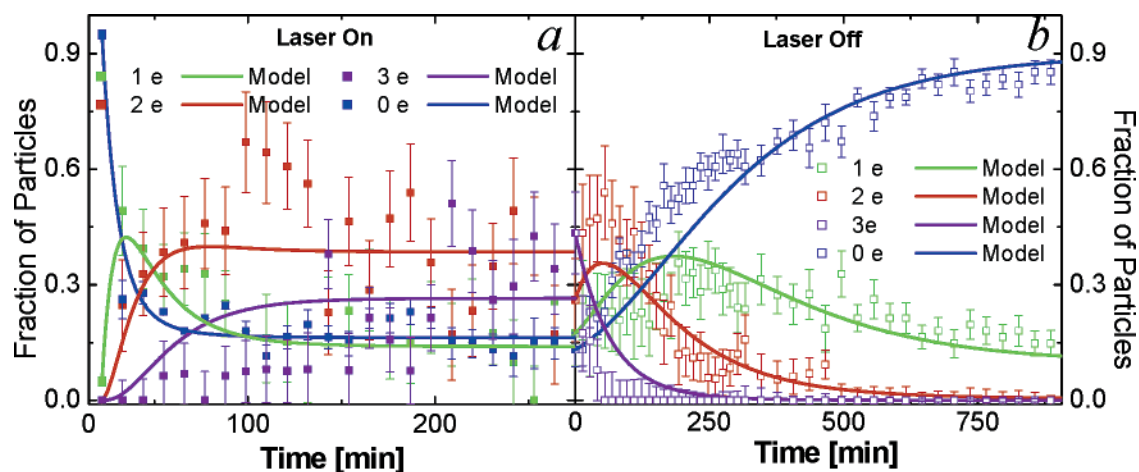
Figure 19. Relative concentrations of particles with 0−3 positive charges as a function of (a) excitation time (396-nm laser on) and (b) relaxation time (laser off) for a sample of nanocrystals on N-type silicon with 14-Å SiO$_2$. The solid curves are fits of a kinetic model described in section 4.4 with corresponding parameters shown in Table 4.1.

sufficiently precise numbers for excited-state lifetimes and excitation intensities and we do not account for the microscopic nature of the Si/SiO$_2$ interface, which plays an increasingly important role in these ultrathin oxides. Some of the observed discrepancies, such as higher-than-expected $k_{tunnel}^{396}/k_{tunnel}^{532}$ ratios,

suggest that resonant tunneling through defect states is important and that there may be some uncertainty in the width or height of the tunneling barrier, which would have a strong effect on the expected value of a, a parameter that appears to be in good agreement with the model.

Photoionization of CdSe/CdS Nanocrystals

J. Phys. Chem. B, Vol. 108, No. 16, 2004 **4959**

TABLE 1: Summary of the Best-Fit Parameters for the Kinetic Model Describing the Photionization and Relaxation of CdSe/CdS Nanoparticles under Various Experimental Conditions

λ [nm]	h_{SiO_2} [Å]	Si [N/P]	photoexcitation						relaxation		
			k_f [min^{-1}]	k_b [min^{-1}]	a	a theory	f	k_b/k_f	k_{off-f} [min^{-1}]	k_{off-b} [min^{-1}]	a_{off}
532	21	N	5.0×10^{-2}	6.0×10^{-3}	1.6	3	0.5	0.1			
532	21	P	1.6×10^{-2}	1.0×10^{-2}	3.3		0.7	0.6			
396	21	N	5.0×10^{-2}	9.0×10^{-3}	1.8	3.6	0.5	0.2	1.0×10^{-4}	2.7×10^{-3}	2.0
396	21	P	4.0×10^{-2}	1.0×10^{-2}	2.2		0.7	0.3	5.5×10^{-3}	1.3×10^{-2}	1.8
532	14	N	2.5×10^{-2}	5.0×10^{-3}	2.0	2	0.6	0.2	8.0×10^{-4}	4.5×10^{-3}	2.5
532	14	P	1.0×10^{-2}	7.0×10^{-3}	2.7		0.6	0.7	4.0×10^{-3}	1.5×10^{-2}	1.3
396	14	N	$1.1 \times 10{-01}$	1.0×10^{-2}	2.0	2.2	0.9	0.1	8.0×10^{-4}	6.0×10^{-3}	1.8
396	14	P	3.5×10^{-2}	2.6×10^{-2}	3.8		0.6	0.7	3.5×10^{-3}	1.6×10^{-2}	2.0

TABLE 2: Tunneling Rates from the 1s (k_{tunnel}^{532}) and 1p (k_{tunnel}^{396}) Excited States, Tunneling Probabilities Per Excitation with 396- and 532-nm Light, and Their Ratios Calculated from the Rate Constant Fits

h_{SiO_2} [Å]	Si [N/P]	k_{tunnel}^{532} [min^{-1}]	k_{tunnel}^{396} [min^{-1}]	$k_{tunnel}^{396}/k_{tunnel}^{532}$	k_f/N_λ (532)	k_f/N_λ (396)	$(k_f^{396}/N_{396})/(k_f^{532}/N_{532})$
21	N	$6.94 \times 10^{+4}$	$1.49 \times 10^{+6}$	$2.14 \times 10^{+1}$	1.0×10^{-5}	1.2×10^{-5}	1.14
14	N	$3.47 \times 10^{+4}$	$2.10 \times 10^{+7}$	$6.04 \times 10^{+2}$	5.2×10^{-6}	2.6×10^{-5}	5.03
21	P	$2.22 \times 10^{+4}$	$6.19 \times 10^{+6}$	$2.79 \times 10^{+2}$	3.3×10^{-6}	9.5×10^{-6}	2.86
14	P	$1.39 \times 10^{+4}$	$6.25 \times 10^{+6}$	$4.50 \times 10^{+2}$	2.1×10^{-6}	8.3×10^{-6}	4.00
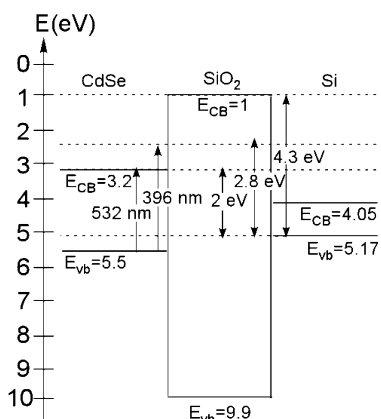
Figure 20. Relative band offsets of CdSe, Si, and SiO$_2$ and the energies of photoexcited electrons with respect to the silicon valence band.

The range of behaviors of individual particles can be more accurately assessed if multiple time traces are obtained for each particle and the probabilities of finding the particle in some state $|+n\rangle$ as a function of time are determined.

6. Discussion and Conclusions

Originally neutral CdSe/CdS core−shell nanoparticles on conductive substrates readily give up electrons when photoexcited even at very low intensities (0.1−0.01 W/cm^2) above their band gap. Quantitative analysis of the z dependence of the charge signals as well as of the cross-sectional line scans suggests that particles can lose between 1 and 5 electrons upon photoexcitation. Line broadening is sometimes observed over time, which may be due to oxide-trapped charges underneath the particles.

A variety of behaviors were observed on all substrates, with some particles charging strongly and gradually, others blinking on and off on faster time scales, and some never charging at all during the course of the experiment. The analysis of the charge signal is complicated by the underlying charge profile of the substrates, especially on N-type silicon. More multiply charged particles are seen on N-type than on P-type substrates independent of other parameters. More uniform behavior is seen on P-type substrates; however, a single strongly charging outlier

was observed, suggesting that local variations in the substrate have a strong influence on nanoparticle photoionization.

The nature of gradual relaxation behavior observed in individual particle charge versus time traces is somewhat unexpected in the context of dealing with the transfer of single elementary charges. Data showing discrete jumps in increments of single electrons would be significantly easier to interpret. However, as we showed in sections 3 and 4 a wide range of signals can be expected from a particle containing even a single charge because of the position of this charge within the particle. It does not seem unreasonable to suggest that the gradual relaxation is due to charges hopping along the traps on the particle surface and tunneling off into the silicon when they reach the bottom of the particle, where the spatial overlap with silicon is the greatest. It is also plausible that charge lingers in the oxide for some time, creating an increased observed signal even after the particle has recovered one of its lost electrons. If the reneutralization mechanism involves charge hopping through trap states in SiO$_2$, then the rate difference between thinner and thicker oxides would be affected more by the proximity of the closest trap sites than by overall oxide thickness, which may explain the relatively weak observed dependence of rates on oxide thickness.

The relative rates for forward and reverse electron transfer were analyzed using a simple four-parameter model and were found to be highly perturbed by the nature of the substrate as well as by the photoexcitation wavelength. Surface band bending due to dangling bond states on N- and P-type silicon substrates causes the ratio of the back to forward electron-transfer rate constants, k_b/k_f, to be larger for P- than for N-type silicon. The relaxation rates in the dark, $k_{off,b}$, are also much faster on the P-type substrate. Dopant type has a stronger effect on $k_{off,b}$ than oxide thickness.

The data used in ensemble kinetics analysis was quite noisy. Systematically poorer agreement of the model with strongly charging systems suggests that highly charging particles follow different kinetics from those that lose only one or two electrons. In addition, only a fraction of the particles within a given sample were active in the photoionization process on the time scale of these experiments, hence the remaining particles must follow much slower kinetics. All together it appears that the substrate is responsible for introducing a trend in the overall photoionization behavior, whereas individual particle kinetics are still

strongly perturbed by their local environment such as the local oxide thickness, density of oxide defect states in the particle's vicinity, and local work function of the silicon as well as the quality of the particle itself.

The higher observed rates of tunneling with 396-nm excitation indicate that the 1P state of the exciton is responsible for faster tunneling. The relative ratios of the tunneling rates for 396- and 532-nm excitations on the same samples are much higher than expected for 14- and 21-Å tunneling barriers. These ratios are larger for thinner oxides, which also contradicts tunneling predictions. This is unexpected because of its much shorter lifetime but may be due to better spatial overlap with the substrate and/or stronger coupling to oxide defects. These observations may be explained by uncertainty in the excitation intensity, the effect of the silicon surface on the absorption cross sections and excited-state lifetimes, and resonant tunneling through defect states.

This experiment is somewhat limited by its inability to observe events that happen on short time scales. However, because our excitation intensities are approximately 5 orders of magnitude lower than those of optical blinking experiments, the events observed in our work should correspond to ~100-ms events observed in single-particle fluorescence studies. An experiment to investigate fluorescence blinking and exciton lifetimes on various silicon substrates analyzed in light of these results may provide more information about the extent of the effect that the electronic structure of the substrate has on particle photoionization.

The extreme sensitivity of these particles to their local environment is somewhat troublesome with regard to their potential applications in single-molecule electronic devices. However, this sensitivity may be quite useful for sensor-type applications, once the behavior is better understood. The fact that we can induce behavioral trends in particle ionization by varying the environment suggests that by carefully controlling the fabrication process we can tune the particle behavior to suit the needs of the application.

Appendix: Modeling Tip−Surface and Tip−Sample Interactions

The probe is modeled as a cone with a sphere at one end as shown in Figure 2. The charge distribution on the probe is determined by its capacitive interactions with the substrate. Because all of the probe components are at the same voltage, $C_{probe-substrate}$ is given by

$$C_{probe-substrate} = C_{sphere-plate} + C_{cone-plate} \quad (A1)$$

In this equation, different terms dominate at different z values. The charge on the sphere portion of the probe is $Q_{sphere} =$

$C_{sphere-plate}V$ located at the center of the sphere. The sphere−plate capacitance is given by

$$C_{sphere-plate} = 4\pi\epsilon_0\rho + 4\pi\epsilon_0\rho\sum_{n=2}^{\infty}\frac{\sin h(\alpha)}{\sin h(n\alpha)} \quad (A2)$$

where

$$\alpha = \ln\left(1 + \sqrt{\frac{z^2}{\rho^2} + \frac{2z}{\rho}} + \frac{z}{\rho}\right)$$

and ρ is the tip radius. The charge distribution on the cone is approximated by a semi-infinite uniform line-charge, with charge density λ starting at position $z_1 = z\sqrt{1+\tan^2\theta}$ and extending to infinity. λ is given by

$$\lambda = \frac{4\pi\epsilon_0 V_{ac}}{\beta} \quad (A3)$$

where

$$\beta = \ln\left(\frac{1 + \cos\theta}{1 - \cos\theta}\right)$$

and θ is the cone angle of the probe.[15,37,38] These parameters are illustrated in Figure 2.

To write down the potential due to a charge within a nanoparticle, we consider them to be polarizable spheres. If charge q is located within a particle a distance s from the particle center (Figure 2) and at an angle ϕ to the substrate-surface normal, x is a radial distance from the surface normal axis going through the center of the particle, and ζ is the height above the nanoparticle center, then the potential at point (x, ζ) is given by

$$\varphi(x, \zeta) = \frac{q}{4\pi\epsilon_0}\sum_{n=0}^{\infty}\left(\frac{s^n}{(\sqrt{x^2 + \zeta^2})^{n+1}}\right)\left(\frac{2n+1}{\epsilon n + n + 1}\right)P_n(\cos\phi_1(x, \zeta)) \quad (A4)$$

where

$$\cos\phi_1(x, \zeta) = \frac{-x\sin\phi + \zeta\cos\phi}{\sqrt{(x\cos\phi + \zeta\sin\phi)^2 + (-x\cos\phi + \zeta\sin\phi)^2}} \quad (A5)$$

Here ϵ is the dielectric constant of the spherical particle, and $P_n(a)$ is the nth-order Legendre polynomial in a.[39] This equation is valid in both the near- and far-field limits. Similarly, the potential at (x, ζ) due to the image particle can be written as

$$\varphi_{im}(x, \zeta) = \frac{q}{4\pi\epsilon_0}\sum_{n=0}^{\infty}\left(\frac{s^n}{(\sqrt{x^2 + \zeta_2^2})^{n+1}}\right)\left(\frac{2n+1}{\epsilon n + n + 1}\right)P_n(\cos\phi_2(x, \zeta)) \quad (A6)$$

where

$$\zeta_2 = \frac{\zeta + d + 2h}{\epsilon_{SiO_2}} \quad (A7)$$

and

$$\cos \phi_2(x, \zeta) =$$

$$\frac{-x \sin[\pi - \phi] + \zeta_2 \cos[\pi - \phi]}{\sqrt{(x \cos[\pi - \phi] + \zeta_2 \sin[\pi - \phi])^2 + (-x \cos[\pi - \phi] + \zeta_2 \sin[\pi - \phi])^2}} \tag{A8}$$

Thus, we can define the potential felt at point (x, ζ) due to an arbitrary discrete charge distribution within a polarizable particle on a conductive substrate as

$$\varphi_{total}(x, \zeta) = \sum_i (\varphi_i(q_i, s_i, \phi_i, x, \zeta) + \varphi_{im,i}(q_i, s_i, \phi_i, x, \zeta)) \tag{A9}$$

where charges q_i have coordinates s_i and ϕ_i. This expression for the potential does not include the polarization of the particle by its own image. However, the error due to this omission should be no more than 5%.[15]

We now define z as the separation between the bottom of the EFM probe and the top plane of the conductive substrate, which is a variable parameter in the experiment. If the surface normal component of the total electric field due to the particle is $-\mathrm{d}/\mathrm{d}\zeta\varphi(x, \zeta)$, then the total force on the probe as a function of tip−surface separation z is given by the sum of the interaction of the probe's point charge and the line charge with this field:

$$F_\omega(x, z) = -2\left(\left[\frac{\mathrm{d}}{\mathrm{d}\zeta}\varphi_{total}\right](x, s_1)Q_{sphere} + \int_{s_2}^\infty \frac{\mathrm{d}}{\mathrm{d}\zeta}\varphi_{total}(x, \zeta)\lambda \, \mathrm{d}\zeta\right)$$

$$= -2\left(\left[\frac{\mathrm{d}}{\mathrm{d}\zeta}\varphi_{total}\right](x, s_1)Q_{sphere} - \varphi_{total}(x, s_2)\lambda\right) \tag{A10}$$

Here the s_i's define the distances between the charges on the tip and the center of the particle (Figure 2) and are given by

$$s_1 = z + \rho - \frac{d}{2} - \frac{h}{\epsilon_h} \tag{A11a}$$

$$s_2 = z_1 + \rho - \frac{d}{2} - \frac{h}{\epsilon_h} \tag{A11b}$$

The factor of 2 comes into eq A10 to account for the interaction of the tip's image with the surface electric field. Now we can substitute eq A10 into eq 1, and using experimental data for $\Delta\nu(\omega)$, we can back out the model parameters such as the charge distribution within a given particle. With these tools, we can analyze both the z dependence and cross sections of the observed electrostatic force gradients.

References and Notes

(1) Nirmal, M.; Dabbousi, B. O.; Bawendi, M. G.; Macklin, J. J.; Trautman, J. K.; Harris, T. D.; Brus, L. E. *Nature* **1996**, *383*, 802.

(2) Shimizu, K. T.; Neuhauser, R. G.; Leatherdale, C. A.; Empedocles, S. A.; Woo, W. K.; Bawendi, M. G. *Phys. Rev. B* **2001**, *6320*, 205316.

(3) Neuhauser, R. G.; Shimizu, K. T.; Woo, W. K.; Empedocles, S. A.; Bawendi, M. G. *Phys. Rev. Lett.* **2000**, *85*, 3301.

(4) Empedocles, S. A.; Neuhauser, R.; Shimizu, K.; Bawendi, M. G. *Adv. Mater.* **1999**, *11*, 1243.

(5) Empedocles, S.; Bawendi, M. *Acc. Chem. Res.* **1999**, *32*, 389.

(6) Empedocles, S. A.; Bawendi, M. G. *Science* **1997**, *278*, 2114.

(7) Banin, U.; Brucher, M.; Alivisatos, A. P.; Ha, T.; Weiss, S.; Chemla, D. S. *J. Chem. Phys.* **1999**, *110*, 1195.

(8) Kuno, M.; Fromm, D. P.; Hamann, H. F.; Gallagher, A.; Nesbitt, D. J. *J. Chem. Phys.* **2001**, *115*, 1028.

(9) Kuno, M.; Fromm, D. P.; Johnson, S. T.; Gallagher, A.; Nesbitt, D. J. *Phys. Rev. B* **2003**, *67*, 125304.

(10) Kuno, M.; Fromm, D. P.; Gallagher, A.; Nesbitt, D. J.; Micic, O. I.; Nozic, A. J. *Nano Lett.* **2001**, *1*, 557.

(11) Mikhailovsky, A. A.; Malko, A. V.; Hollingsworth, J. A.; Bawendi, M. G.; Klimov, V. I. *Appl. Phys. Lett.* **2002**, *80*, 2380.

(12) Malko, A. V.; Mikhailovsky, A. A.; Petruska, M. A.; Hollingsworth, J. A.; Htoon, H.; Bawendi, M. G.; Klimov, V. I. *Appl. Phys. Lett.* **2002**, *81*, 1303.

(13) Michalet, X.; Pinaud, F.; Lacoste, T. D.; Dahan, M.; Bruchez, M. P.; Alivisatos, A. P.; Weiss, S. *Single Mol.* **2001**, *2*, 261.

(14) Cherniavskaya, O.; Chen, L.; Islam, M. A.; Brus, L. E. *Nano Lett.* **2003**, *3*, 497.

(15) Cherniavskaya, O.; Chen, L.; Weng, V.; Yuditsky, L.; Brus, L. E. *J. Phys. Chem. B* **2003**, *107*, 1525.

(16) Albrecht, T. R.; Grutter, P.; Horne, D.; Rugar, D. *J. Appl. Phys.* **1991**, *69*, 668.

(17) Peng, X. G.; Schlamp, M. C.; Kadavanich, A. V.; Alivisatos, A. P. *J. Am. Chem. Soc.* **1997**, *119*, 7019.

(18) Krauss, T. D.; O'Brien, S.; Brus, L. E. *J. Phys. Chem. B* **2001**, *105*, 1725.

(19) Krauss, T. D.; Brus, L. E. *Mater. Sci. Eng., B* **2000**, *69–70*, 289.

(20) van Sark, W.; Frederix, P. L. T. M.; van den Heuvel, D. J.; Gerritsen, H. C. *J. Phys. Chem. B* **2001**, *105*, 8281.

(21) Sader, J. E.; Chon, J. W. M.; Mulvaney, P. *Rev. Sci. Instrum.* **1999**, *70*, 3967.

(22) The other histograms were not shown here only in the interest of space conservation.

(23) We do not know that the location of electrons within the particles is distributed as a Gaussian. But because of the lack of other information, a Gaussian distribution is used.

(24) This number was ~0.3 V for the substrates used in our previous study. One substantial difference observed during the course of these experiments as compared to the prior work is that at this time no negative particles were observed.

(25) Wang, L.-W.; Zunger, A. *Phys. Rev. B* **1996**, *53*, 9579.

(26) Hirose, M. *Mater. Sci. Eng., B* **1996**, *41*, 35.

(27) Shimizu, K. T.; Woo, W. K.; Fisher, B. R.; Eisler, H. J.; Bawendi, M. G. *Phys. Rev. Lett.* **2002**, *89*, art. no. 117401.

(28) Klimov, V. I.; Mikhailovsky, A. A.; McBranch, D. W.; Leatherdale, C. A.; Bawendi, M. G. *Phys. Rev. B* **2000**, *61*, R13349.

(29) Schlegel, G.; Bohnenberger, J.; Potapova, I.; Mews, A. *Phys. Rev. Lett.* **2002**, *88*, art. no.

(30) Stavola, M.; Dexter, D. L.; Knox, R. S. *Phys. Rev. B* **1985**, *31*, 2277.

(31) Green, M. L.; Gusev, E. P.; Degraeve, R.; Garfunkel, E. L. *J. Appl. Phys.* **2001**, *90*, 2057.

(32) Lucovsky, G.; Wu, Y.; Niimi, H.; Yang, H.; Keister, J.; Rowe, J. E. *J. Vac. Sci. Technol., A* **2000**, *18*, 1163.

(33) Gusev, E. P.; Lu, H.-C.; Gustafsson, T.; Green, M. L. *IBM J. Res. Dev.* **1999**, *43*, 265.

(34) Stadele, M.; Tuttle, B. R.; Hess, K. *J. Appl. Phys.* **2001**, *89*, 348.

(35) Neaton, J. B.; Muller, D. A.; Ashcroft, N. W. *Phys. Rev. Lett.* **2000**, *85*, 1298.

(36) Enderlein, R.; Horing, N. J. M. *Fundamentals of Semiconductor Physics and Devices*; World Scientific: Singapore, 1997.

(37) Belaidi, S.; Girard, P.; Leveque, G. *J. Appl. Phys.* **1997**, *81*, 1023.

(38) Kalinin, S. V.; Bonnell, D. A. *Phys. Rev. B* **2000**, *62*, 10419.

(39) Bottcher, C. J. F. *Dielectrics In Static Fields*, 2nd ed.; Elsevier: Amsterdam, 1973; Vol. 1.